Inorganic Chemistry

Article

pubs.acs.org/IC

Synthesis of the Layered Quaternary Uranium-Containing Oxide $Cs_2Mn_3U_6O_{22}$ and Characterization of its Magnetic Properties

Cory M. Read,[†] Elijah E. Gordon,[‡] Mark D. Smith,[†] Jeongho Yeon,[†] Gregory Morrison,[†] Myung-Hwan Whangbo,[‡] and Hans-Conrad zur Loye*[,†]

[†]Department of Chemistry and Biochemistry, University of South Carolina, Columbia, South Carolina 29208, United States

[‡]Department of Chemistry, North Carolina State University, Raleigh, North Carolina 27695, United States

Supporting Information

ABSTRACT: A layered quaternary uranium-containing oxide, $Cs_2Mn_3U_6O_{22}$, was crystallized from a cesium chloride flux. The crystal structure was determined to consist of α-U_3O_8 topological layers that are separated by alternating cesium and manganese layers. This ordered arrangement creates a separation between manganese layers of 13 Å, leading to complex low-dimensional magnetic properties. The compound crystallizes in a new structure type in the monoclinic space group, $C2/m$, with a = 6.8730(10) Å, b = 11.7717(17) Å, c = 13.374(2) Å, and β = 99.673(5)°. The magnetic properties were measured and analyzed by first-principles density functional theory calculations.

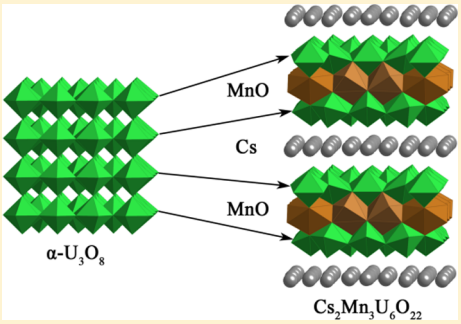

1. INTRODUCTION

Structures and properties are closely intertwined in solid-state materials, and often, specific structural features are necessary for effecting certain properties. Creating such structural features as well as improving upon what exists in known structures requires the synthesis of new structure types and concomitant compositions, often via a synthetic strategy aimed at materials discovery. A chemical composition that adopts a new structure type, in particular, when it possess unique chemical environments, can lead to interesting physical phenomena. For example, structural features, such as chains or layers, that can act to enhance or prevent interactions between magnetic elements in a structure, can result in unique magnetic behavior.[1−8] This is often observed for layered compounds when magnetic cations are confined to within the layers, which leads to low-dimensional magnetic behavior when the layers are well-separated.[9−16] In such materials, the strengths of the intralayer spin exchange interactions lead to a short-range magnetic order, while the interlayer spin exchange interactions determine whether or not the material will exhibit long-range magnetic ordering. When the interlayer interactions are very weak, no long-range magnetic order takes place down to the lowest temperatures measurable unless the layer is an Ising magnet (i.e., it has a nonzero magnetic moment only in one direction).[17]

The creation of low-dimensional magnetic systems, therefore, requires a combination of structural components that function either as magnetic layers that contain the magnetic ions or as separators that isolate the magnetic layers from each other. The separators should not contain any magnetic ions and, generally speaking, the thicker the separator is, the less communication will take place between the magnetic layers. Often separating the magnetic layers by more than 5 Å will result in a noticeable decrease in the magnetic coupling between the magnetic layers and, as the layer thickness increases, the coupling continues to decrease. At some limit, the magnetic layers would be truly isolated and, if thin enough, exhibit strictly low-dimensional magnetic behavior.

Uranium oxides have not typically been investigated for their magnetic properties as U^{6+} has an f^0 electron configuration and is nonmagnetic, and U^{4+} (f^2)-containing oxides are extremely rare. However, as shown in this paper, U^{6+} cations can connect into sheet structures that both act as separators and as structure directing agents that promote the formation of layered structures.

A significant number of uranium-containing oxides have been prepared, and their structures have been published since uranium is of interest for its atomic structure and fissile abilities.[18] Not surprisingly, while binary and ternary phases have been extensively investigated, far fewer quaternary uranium-containing oxides, other than minerals, are known and have been investigated.[19] The simplest oxides are the binaries UO_2, U_3O_8, and UO_3, which contain uranium in oxidation states of +4, +5/+6, and +6, respectively. These binaries exhibit unique structural features that sometimes are found in more complex structures, and are typically a function of the uranium oxidation state. U^{6+} typically exists in the ubiquitous UO_2^{2+} uranyl species, which contains short U═O bonds and long U−O bonds arranged in square, pentagonal, and hexagonal bipyramidal coordination environments, where the short uranyl U═O bonds are axial and the longer U−O

Received: March 10, 2015
Published: May 8, 2015

DOI: 10.1021/acs.inorgchem.5b00552
Inorg. Chem. 2015, 54, 5495−5503

bonds are equatorial.[20] In many cases, these bipyramids share edges and corners to form layers, where the axial uranyl oxygens can bond either to other uranium cations, called a cation−cation-interaction (CCI), or to other nonuranium metal cations. An example of the former is the structure of α-U_3O_8, which contains sheets of edge sharing UO_7 polyhedra that connect in the *c*-direction via shared uranyl oxygen. These and other sheet structures have been found in some uranium-containing oxides where they occur as isolated layers and create distinct complex layered oxide structures.[19] These isolated layers represent a potential building block for structures exhibiting low-dimensional magnetism if other nonmagnetic layers can be inserted to create long distances between magnetic layers, as found for the title compound.

To explore the synthesis of layered structures that can promote low-dimensional magnetic behavior, we used the flux growth method, which is a proven method for exploratory crystal growth[21] and which has proven itself to be an effective approach for the growth of uranium-containing oxides. Common fluxes include alkali-metal hydroxide and carbonate fluxes that work well for the crystal growth of complex oxides, including uranium-containing oxides.[22−28] Recently, we found that halide fluxes promote the formation of uranium-containing oxides[29] as well as altogether novel compositions.[30−33] Many of the new compositions that were synthesized using this approach contain first row transition metals, in addition to the uranium, which led us to further utilize these fluxes for exploratory crystal growth of complex uranium oxides containing 3d transition metals.

In the present work, we report on a new, layered quaternary uranium-containing oxide, $Cs_2Mn_3U_6O_{22}$, prepared as single crystals using the flux crystal growth method.[21] This layered structure contains isolated manganese-containing magnetic layers that give rise to unusual magnetic behavior. We examined its structure by scanning electron microscopy (SEM) and single-crystal X-ray diffraction (XRD), characterized its magnetic structure by magnetic susceptibility and magnetization measurements, and investigated its electronic and magnetic structures by first-principles density functional theory (DFT) calculations.

2. EXPERIMENTAL SECTION

Reagents. U_3O_8 (International Bioanalitics Industries Inc., ACS grade), $MnCl_2{\cdot}4H_2O$ (Alfa Aesar, 99%), and CsCl (Alfa Aesar, 99%) were used as received. ***Caution!*** *Although the uranium precursors used contain depleted uranium, standard safety measures for handling radioactive substances should be followed.*

Synthesis. Single crystals of the title compound were grown from a molten cesium chloride flux. 1 mmol $MnCl_2{\cdot}4H_2O$, 0.33 mmol U_3O_8, and 10 mmol CsCl were added to an alumina crucible. The reactants were heated at a rate of 20 °C/min to 900 °C, held there for 9 h, and cooled to room temperature by turning the furnace off. The majority of the flux evaporates during the course of the reaction, thereby promoting crystal growth. The crystals were isolated from the remaining CsCl by quickly washing with water, assisted by sonication. The reaction yielded ∼40% large platelike crystals of the title compound along with smaller crystals and some black, polycrystalline material, which could not be positively identified. Although the yield of $Cs_2Mn_3U_6O_{22}$ could be optimized, it was not possible to eliminate the simultaneous formation of smaller crystals and of the black, polycrystalline material. A phase-pure sample for physical property measurements was obtained by manual separation. Phase purity was confirmed by powder X-ray diffraction (Supporting Information, Figure S1).

Single-Crystal X-ray Diffraction. Crystals of the compound grow as orange plates with rounded edges and corners, suggesting partial dissolution in the flux after crystal formation. Difficulty was encountered in selecting a high-quality data crystal. Several (ca. 20) crystals were examined at room temperature and at low-temperature; most exhibited high mosaicity as indicated by broad diffraction maxima profiles, which frequently had long "tails". Ultimately, data sets from four different crystals were collected; the structural features of all were comparable, and the best is reported here. The slightly wide and asymmetric peak profiles observed in all data crystals are attributable to cation disorder (see below). During the course of studies of the candidate crystals, the room- and low-temperature unit cells were found to be unchanged except for the expected thermal contraction/expansion; no phase transition behavior was observed in the range of 100−294 K. The X-ray intensity data were collected at 100(2) K using a Bruker SMART APEX diffractometer (Mo Ka radiation, l = 0.710 73 Å)[34] on a small crystal with approximate dimensions 0.05 × 0.04 × 0.02 mm^3. The data collection consisted of seven separate ω-scans at different 2θ and φ angular settings as well as one additional φ-scan. The data collection covered 99.4% of the reciprocal space to $2\theta_{max}$ = 66.2°, with an average reflection redundancy of 6.1 to $2\theta_{max}$ and R_{int} = 0.065 after absorption correction. The raw area detector data frames were reduced and corrected for absorption effects using the SAINT+ and SADABS programs.[34] The SADABS absorption correction reduced the R_{int} value from ca. 22.5% to 6.5%. Final unit cell parameters were determined by least-squares refinement of 2053 reflections from the data set. The structure was solved by direct methods using SHELXS.[35] Subsequent difference Fourier calculations and full-matrix least-squares refinement against F^2 were performed with SHELXL as implemented in OLEX2.[36] Crystallographic data, atomic coordinates, and selected interatomic distances are listed in Tables 1, 2, and 3, respectively, and anisotropic displacement parameters are compiled in Supporting Information, Table S1. The atomic composition based on energy-dispersive spectroscopy (EDS) analysis of several crystals was consistent with an elemental ratio of Cs = 2.0(1), Mn = 3.0(1), and U = 6.0(1).

Powder X-ray Diffraction. Powder XRD data were collected on a Rigaku D/Max-2100 powder X-ray diffractometer using Cu Kα radiation. The step-scan covered the 2θ angular range of 5−70° in

Table 1. Crystal Data and Structure Refinement for cr1105cs

empirical formula	$Cs_{2.02}Mn_3O_{22}U_6$
formula weight	2212.91
temperature/K	100(2)
crystal system	monoclinic
space group	*C*2/*m*
a/Å	6.8730(10)
b/Å	11.7717(17)
c/Å	13.374(2)
β/deg	99.673(5)
volume/Å^3	1066.6(3)
Z	2
ρ_{calc} mg/mm^3	6.890
m/mm^{-1}	50.565
F(000)	1828.0
crystal size/mm^3	0.05 × 0.04 × 0.02
2θ range for data collection	3.08 to 66.24°
index ranges	$-10 \le h \le 10$, $-17 \le k \le 18$, $-20 \le l \le 20$
reflections collected	15 527
independent reflections	2130 [R(int) = 0.0654]
data/restraints/parameters	2130/0/97
goodness-of-fit on F^2	1.098
final R indexes [$I \ge 2\sigma$ (I)]	R_1 = 0.0380, wR_2 = 0.0862
final R indexes [all data]	R_1 = 0.0476, wR_2 = 0.0899
largest diff. peak/hole/ e^{-1}/Å^{-3}	5.97/−4.35

DOI: 10.1021/acs.inorgchem.5b00552
Inorg. Chem. 2015, 54, 5495−5503

Table 2. Fractional Atomic Coordinates (1×10^4) and Equivalent Isotropic Displacement Parameters ($Å^2 \times 10^3$)

atom	sof	x	y	z	U^a (eq)
U1		4153.3(4)	1773.2(2)	2064.4(3)	10.73(9)
U2		8829.7(6)	0	2029.0(4)	10.99(11)
Mn1		0	1512.0(18)	0	23.2(4)
Mn2	0.50	5000	140(20)	0	24(4)
Cs1	0.392(4)	8414(3)	1597.0(17)	4934.9(15)	33.3(7)
Cs2	0.223(6)	6716(11)	0	4957(4)	55(2)
O1		2447(9)	3345(5)	2265(6)	17.1(13)
O2		10912(9)	1306(6)	1707(6)	24.2(15)
O3		4354(12)	1522(6)	3402(7)	27.6(17)
O4		3801(12)	1963(7)	652(6)	27.1(16)
O5		8145(13)	0	510(8)	20.2(19)
O6		9744(16)	0	3363(8)	26(2)
O7		4983(12)	0	1671(8)	18.9(19)

[a] U_{eq} is defined as 1/3 of of the trace of the orthogonalised U_{ij} tensor.

steps of 0.02°. Because of the plate crystal morphology, significant preferred orientation effects are observed. No impurities were observed, and the calculated and experimental PXRD patterns on ground crystals are in excellent agreement (see Supporting Information, Figure S1).

Scanning Electron Microscopy. Scanning electron micrographs of single crystals of $Cs_2Mn_3U_6O_{22}$ were obtained using a Tescan Vega-3 SEM instrument utilized in low-vacuum mode. An SEM image of a representative crystal of $Cs_2Mn_3U_6O_{22}$ is shown in Figure 1. Elemental analysis was performed on single crystals using a Thermo EDS instrument. The crystals were mounted on carbon tape and analyzed using a 30 kV accelerating voltage and an accumulation time of 20 s. As a qualitative measure, EDS verified the presence of the uranium, manganese, cesium, and oxygen and did not indicate the presence of other elements.

Magnetic Measurements. Magnetic properties were measured on a Quantum Design Magnetic Property Measurement System (QD MPMS 3 SQUID Magnetometer). Temperature dependent susceptibility data was measured on ground crystals of known mass loaded into a VSM powder holder. Magnetic susceptibility data was measured with an applied field of 1,000 Oe from 2−300 K under zero-field cooled (ZFC) and field cooled (FC) conditions. Further zero-field cooled magnetization measurements were performed with H = 100, 5,000 and 20,000 Oe. The raw magnetic moments were corrected for sample shape and radial offset effects using the method reported by Morrison and zur Loye.[37] The temperature dependence of the magnetic susceptibility was also measured on oriented single crystals. Several single crystals of unknown mass were stacked onto a strip of Kapton tape using GE 7031 Varnish. Measurements with H parallel to the thin macroscopic axis of the crystals were made by taping the Kapton across the opening of half a gelatin capsule and inserting it into a straw. Measurements with H perpendicular to the thin macroscopic axis of the crystals were obtained by attaching the Kapton tape to a quartz paddle. For both orientations, magnetic susceptibility was measured at an applied field of 1,000 Oe from 2−300 K under zero-field cooled and field cooled conditions. Because the mass of the single crystals was small and unknown, the data for both orientations were normalized using the value measured for the polycrystalline sample at 300 K.

Density Functional Theory Electronic Structure Calculations. We optimized the crystal structure of $Cs_2Mn_3U_6O_{22}$ for its ferromagnetic state by adopting an ordered arrangement of Cs^+ cations shown in Supporting Information, Figure S2 on the basis of spin-polarized DFT calculations. Our calculations for the (2*a*, *b*, *c*) supercell of $Cs_2Mn_3U_6O_{22}$ employ the projected augmented wave (PAW) method encoded in the Vienna ab initio simulation package (VASP),[38−40] the generalized gradient approximation (GGA) of Perdew, Burke, and Ernzerhof[41] for the exchange-correlation correction with the plane wave cutoff energy of 520 eV, a set of 4 × 2 × 2 *k*-points, and the threshold 1×10^{-6} eV for self-consistent-field energy convergence. To describe the electron correlation associated with Mn 3d states, the DFT plus on-site repulsion U (DFT+U) method[42] was applied with $U^{eff} = U - J = 4$ eV. In this structure optimization, we kept constant the unit cell parameters but relaxed all the atom positions with force convergence threshold of 0.02 eV/Å. The optimized atom positions are summarized in Supporting Information, Table S2.

3. RESULTS AND DISCUSSION

A. Synthesis and Crystal Structure. The experimental conditions, temperature, soak time, cooling rate, etc., were systematically varied to identify the conditions where crystal growth was optimized. As the CsCl flux has an appreciable vapor pressure at 900 °C, close to its boiling point of 1297 °C, flux loss was inevitable when that temperature was maintained for any appreciable period of time. Interestingly, the best crystals were obtained when the flux substantially evaporated during the soak time, suggesting that a necessary degree of supersaturation was thereby achieved that resulted in crystal formation. The air- and water-stable crystals formed as pseudohexagonal plates shown in Figure 1.

The compound crystallizes in the monoclinic system. The space groups *C*2, *Cm*, and *C*2/*m* were consistent with the pattern of systematic absences in the intensity data. The best description of the symmetry of the disordered structure is space group *C*2/*m*. The asymmetric unit in *C*2/*m* consists of atomic positions for two cesium atoms, two uranium atoms, two manganese atoms, and seven oxygen atoms. Cesium atom Cs(1), uranium atom U(1), and oxygen atoms O(1)−O(4) are located on general positions (site 8*j*). Cesium atom Cs(2), uranium atom U(2), and oxygen atoms O(5), O(6), and O(7) are located on mirror planes (Wyckoff site symbol 4*i*). Manganese atoms Mn(1) and Mn(2) are located on twofold axes of rotation (site 4*g*). All atoms refined normally with anisotropic displacement parameters except for Mn(2) and both cesium atoms, which require further comments:

(1) Mn(2) split position: In the early refinement stages manganese Mn(2) was placed on site 2*b* (site symmetry 2/*m*). This resulted in a highly prolate anisotropic displacement parameter (ADP) for Mn(2), with $U_3/U_1 = 6.2$ and a coordination sphere consisting of four short Mn−O bonds (2 × 2.16 and 2 × 2.23 Å) and four long equivalent Mn−O(4) bonds of 2.649 Å. Displacing Mn(2) away from the center of the 2/*m* coordination site onto the 4*g* site (site symmetry 2) results in twofold

DOI: 10.1021/acs.inorgchem.5b00552
Inorg. Chem. 2015, 54, 5495−5503

Table 3. Selected Interatomic Distances

atom	atom	length/Å
U1	O1[a]	2.238(6)
U1	O1	2.231(6)
U1	O2[b]	2.646(7)
U1	O2[c]	2.266(6)
U1	O3	1.795(9)
U1	O4	1.877(8)
U1	O7	2.249(4)
U2	O1[d]	2.213(6)
U2	O1[a]	2.213(6)
U2	O2[e]	2.191(7)
U2	O2	2.191(7)
U2	O5	2.007(10)
U2	O6	1.788(11)
U2	O7	2.606(8)
Mn1	O2[c]	2.277(8)
Mn1	O2[f]	2.277(8)
Mn1	O4[g]	2.214(8)
Mn1	O4	2.665(8)
Mn1	O4[h]	2.665(8)
Mn1	O4[b]	2.214(8)
Mn1	O5[i]	2.356(6)
Mn1	O5[c]	2.356(6)
Mn2	O4[i]	2.80(2)
Mn2	O4	2.51(2)
Mn2	O4[f]	2.51(2)
Mn2	O4[e]	2.80(2)
Mn2	O5[i]	2.161(9)
Mn2	O5	2.161(9)
Mn2	O7[i]	2.243(11)
Mn2	O7	2.243(11)
Cs1	O1[a]	3.522(8)
Cs1	O3[j]	3.161(8)
Cs1	O3[a]	3.157(8)
Cs1	O3[k]	3.325(9)
Cs1	O3	3.174(9)
Cs1	O6	3.072(9)
Cs1	O6[l]	3.058(8)
Cs2	O3[e]	3.007(9)
Cs2	O3[j]	3.018(10)
Cs2	O3[m]	3.018(10)
Cs2	O3[n,o,p]	3.007(9)
Cs2	O6	3.220(13)
Cs2	O6[l]	3.022(12)

[a] 1/2 + x,1/2 − y,+z. [b] −1/2 + x,1/2 − y,+z. [c] −1 + x,+y,+z. [d] 1/2 + x,−1/2 + y,+z. [e] +x,−y,+z. [f] 1 − x,+y,−z. [g] 1/2 − x,1/2 − y,−z. [h] −x,+y,−z. [i] 1 − x,−y,−z. [j] 1 − x,+y,1 − z. [k] 3/2 − x,1/2 − y,1 − z. [l] 2 − x,−y,1 − z. [m] 1 − x,−y,1 − z. [n] −1/2 + x,1/2 + y,+z. [o] 1 + x,+y,+z. [p] 2 − x,+y,1 − z.

disorder about a mirror plane, with each half-occupied Mn(2) site displaced toward two symmetry-equivalent O(4) atoms. The coordination sphere now consists of four short Mn−O bonds (2 × 2.162 (O5) and 2 × 2.240 (O7) Å), and two 2.505 Å and two 2.795 Å Mn−O(4) distances. The Mn(2) ADP with the split-position model is much less prolate, with U_3/U_1 = 3.5.

(2) Cesium atoms: Refinement of the two unique cesium atom positions with full site occupancies resulted in poor agreement factors ($R1$ > 0.10), very large displacement parameters (average Cs U_{eq} = 0.15 Å^2), and large electron density holes at the Cs sites. Free refinement of the cesium atoms site occupation factors (sof) gave 0.392(4) for Cs(1) and 0.223(6) for Cs(2), a precipitous drop in R values and a flattened difference map. The refined occupancy values generate the composition $Cs_{2.02(2)}Mn_3U_6O_{22}$, which obeys crystal electroneutrality (within experimental error) assuming U^{6+} and Mn^{2+}. Anisotropic refinement of the two unique cesium atoms yielded oblate ADPs, with U_3/U_1 = 4.5 for Cs(1) and 4.4 from Cs(2), suggesting some positional disorder about the reported sites. Trial disorder models with each Cs atom slightly displaced from a central position were not stable and did not improve the refinement statistics. For the final cycles, each cesium atom was not modeled with a split position but with one anisotropic atomic position, which represents an average of several lesser-occupied components distributed in a disk-shaped arrangement around the reported position. The largest residual electron density peak and hole in the final difference map are +5.97 and −4.35 e$^-$/Å^3, located 0.69 Å from U(2) and 1.64 Å from Cs(2), respectively.

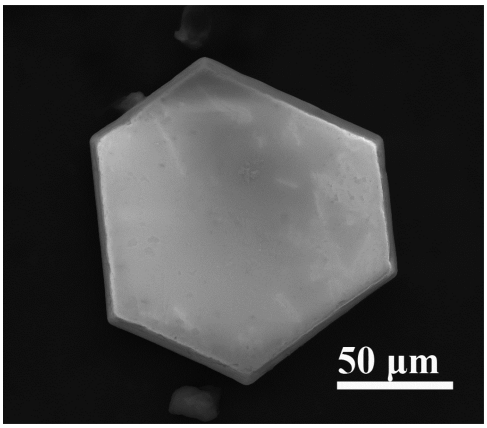

Figure 1. (a) SEM image of $Cs_2Mn_3U_6O_{22}$.

$Cs_2Mn_3U_6O_{22}$ forms in a novel layered structure type consisting of $Mn_3U_6O_{22}^{2-}$ slabs separated by layers of cesium atoms (Figure 2a). Each slab consists of a layer containing

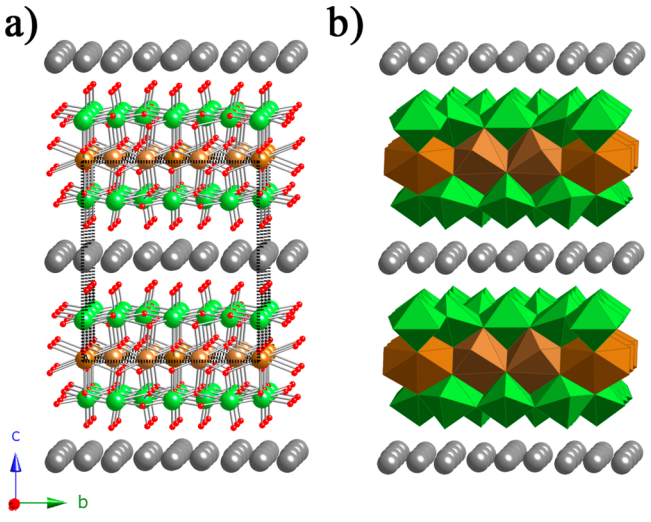

Figure 2. Ball-and-stick (a) and polyhedral (b) representations of $Cs_2Mn_3U_6O_{22}$. Uranium atoms are shown in green, manganese atoms in brown, cesium atoms in gray, and oxygen atoms in red.

DOI: 10.1021/acs.inorgchem.5b00552
Inorg. Chem. 2015, 54, 5495−5503

Mn^{2+} (d^5) ions, sandwiched between layers containing U^{6+} (f^0) ions. The manganese layers are thus separated from each other by two intervening uranium oxide layers and by one cesium layer, creating a large 13 Å separation between Mn layers. A polyhedral representation of the structure is shown in Figure 2b. The uranium layers are structurally related to the layers found in α-U_3O_8, where uranium is located in pentagonal bipyramidal coordination environments. However, while the uranium in α-U_3O_8 is mixed valent U^{6+}/U^{5+}, the uranium in $Cs_2Mn_3U_6O_{22}$ is strictly U^{6+}. The α-U_3O_8-type layers contain edge- and corner-sharing pentagonal bipyramids and are planar, as shown in Figure 3a. There are two uranium positions in this

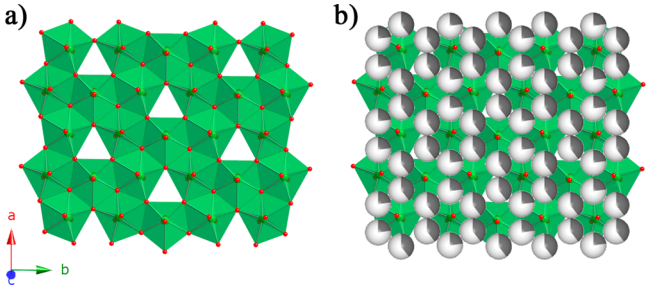

Figure 3. α-U_3O_8-type layer containing uranium in pentagonal bipyramidal coordination environments (a) and the arrangement of cesium atoms between the α-U_3O_8-type layers (b). There are three crystallographic sites that can be occupied by cesium between the layers. However, because of the large size of the cesium cation, they cannot all be occupied at the same time. For this reason, each position has a partial occupancy amounting to two cesium cations distributed over three positions. The Cs1 site has an occupancy of 0.392(4) and Cs2 of 0.223(6).

sheet structure, and both are found in a pentagonal bipyramidal coordination environments, where the short axial U−O bonds, 1.79−2.00 Å, and the long U−O equatorial bonds, 2.19−2.64 Å, are typical for a classical uranyl coordination environment. In α-U_3O_8 the axial oxygens of the uranium pentagonal bipyramids are shared between adjacent uranium layers, a type three cation−cation-interaction,[20] while in $Cs_2Mn_3U_6O_{22}$, the axial oxygens are shared with the manganese and cesium cation layers that separate the uranium layers. Crystallographically, three cations can be accommodated between the uranium layers and be coordinated to the axial oxygens, as happens in the case of manganese. However, the Cs^+ cations are so large that only two cesium cations can be accommodated by partially occupying the three crystallographic sites. Two cesium cations are distributed over three sites, and their partial occupancies are listed in Table 2. In Figure 3b, the cesium atoms are shown as occupying all three sites with the shading on the spheres indicating the degree of site occupancy. The cesium atoms are in a slightly distorted trigonal prismatic coordination environment; however, Cs1 has an additional long 3.522(8) Å bond to O1 that creates a monocapped trigonal prism. Aside from the single long bond, the bonds in the trigonal prism range from 3.007(9) to 3.325(9) Å. The three sites occupied by the cesium cations create face-sharing trigonal prisms, where it is unlikely that both trigonal prisms can be occupied simultaneously, contributing to the reduced cesium occupancy of the layer.

A unit cell of the layer cannot accommodate three Cs^+ cations because of their large size. In contrast, because of their significantly smaller size, three Mn^{2+} cations can be accommodated between the two uranium oxide layers, and a polyhedral representation of their arrangement, filling all the crystallographic sites, is shown in Figure 4a,b. The two

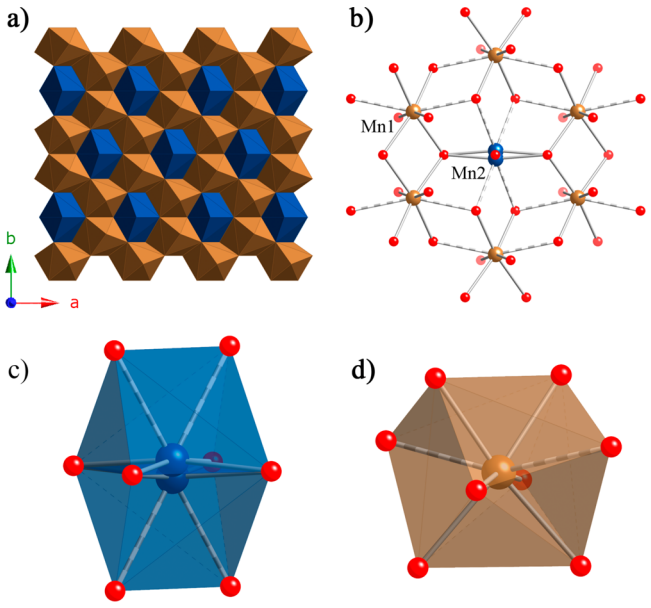

Figure 4. Polyhedral (a) and ball-and-stick (b) representations of the manganese layer in $Cs_2Mn_3U_6O_{22}$ and manganese 6 + 2 coordination environments for Mn2 (c) and Mn1 (d). The irregular polyhedra have a range of Mn−O bond lengths varying from 2 × 2.214, 2 × 2.278, 2 × 2.356, and 2 × 2.665 Å for Mn1 to 2 × 2.162, 2 × 2.240, and 2 × 2.505 and 2 × 2.795 Å for Mn2 (Mn2 occupies a split position). The long Mn−O4 bond lengths are displayed with stripes.

crystallographic sites occupied by manganese are shown separately in Figure 4c,d and combined into one filled layer in Figure 4a. The filling of the layer by all manganese cations creates numerous short Mn−O−Mn connections through which the manganese cations can couple magnetically (see below).

The manganese coordination environments are irregular and are best described as a 6 + 2 coordination environment as shown in Figure 4c,d. The irregular polyhedra have a range of Mn−O bond lengths varying from 2 × 2.214, 2 × 2.277, 2 × 2.356, and 2 × 2.665 Å for Mn1 to 2 × 2.161, 2 × 2.243, 2 × 2.507 and 2 × 2.795 Å for Mn(2). (Mn(2) occupies a split position and there are therefore two sets of bond lengths−only one is listed here.) Mn(2) is displaced away from the center of the 2/*m* coordination site onto the 4*g* site (site symmetry 2), which results in twofold disorder about a mirror plane, with each half-occupied Mn(2) site displaced toward two symmetry-equivalent O(4) atoms. Supporting Information, Figure S3 highlights the connectivity between the manganese cations and the coordination environments that are implied if the Mn−O bond lengths are allowed to increase to include the Mn(1)−O bond of 2.665 Å.

An interesting feature in the crystal structure of $Cs_2Mn_3U_6O_{22}$ is the Mn−O bond lengths, which are all longer than 2.2 Å. Such long Mn−O bonds are also found in $Rb_2MnU_3O_{11}$,[19] $K_2MnU_3O_{11}$,[19] and $MnNb_3O_6$.[43] To verify that the long Mn−O bonds of $Cs_2Mn_3U_6O_{22}$ are intrinsic and not a crystal structure refinement artifact, we optimized the crystal structure of $Cs_2Mn_3U_6O_{22}$ on the basis of DFT+U calculations by adopting an ordered arrangement of Cs^+ cations shown in

DOI: 10.1021/acs.inorgchem.5b00552
Inorg. Chem. 2015, 54, 5495−5503

Supporting Information, Figure S2. The optimized atom positions, summarized in Supporting Information, Table S2 are quite similar to those found experimentally showing that the long Mn−O bonds of $Cs_2Mn_3U_6O_{22}$ are genuine.

The bond valence sums (BVSs)[44] for the Mn1 and Mn2 of $Cs_2Mn_3U_6O_{22}$, using the optimized atom positions, were calculated as follows:

$$\mathrm{BVS} = \sum_{i} \exp\left(\frac{r_0 - r_i}{0.37}\right) \quad (1)$$

where r_0 is the reference length (1.790 Å) for the Mn^{2+}−O^{2-} bond, and r_i is the actual length of the Mn−O bond i surrounding the Mn. Our calculations show that the BVS of Mn1 with its eight Mn1−O bonds is +1.698, and that of Mn2 with its eight Mn2−O bonds is +1.747. Likewise, the BVS of Mn in $MnNb_3O_6$ calculated by using its eight Mn−O bonds 2 × 2.230, 2 × 2.224, and 4 × 2.567 Å is also smaller than +2 (i.e., +1.718). These observations should not be construed as an indication that the oxidation states of the Mn atoms are lower than +2.

In $Cs_2Mn_3U_6O_{22}$ and $MnNb_3O_6$, all O atoms coordinated to the Mn^{2+} ions are shared with other cations A^{n+} (e.g., U^{6+}; Nb^{3+}, Nb^{4+}) of higher oxidation states to form Mn^{2+}−O^{2-}−A^{n+} linkages. In such linkages, some electron density of the Mn−O bond would be shifted toward the A−O region, thereby weakening the Mn−O bond. From the viewpoint of electronic structures, this implies that the filled regions of the O 2s and O 2p states in those oxides are expected to have substantial contributions of the formally empty orbitals of the A^{n+} cations. Indeed, this is the case, as can be seen from the plot of the total and projected density of states (DOS) calculated for $Cs_2Mn_3U_6O_{22}$ (Figure 5).

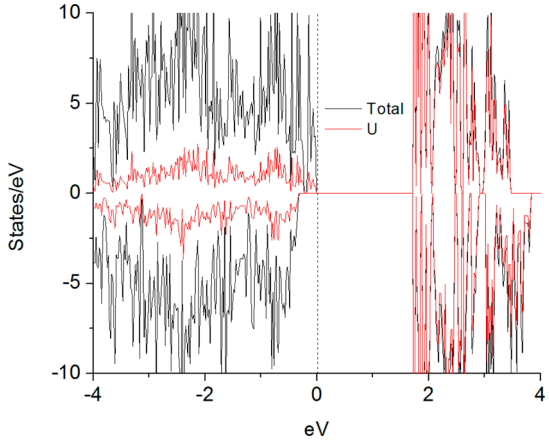

Figure 5. Plots of the total DOS (solid black line) and the PDOS of uranium (red solid line) calculated for $Cs_2Mn_3U_6O_{22}$. The DOS and PDOS values are normalized per Mn, that is, per one-third the formula unit.

B. Magnetic Properties. The magnetic properties of $Cs_2Mn_3U_6O_{22}$ were investigated to ascertain if the isolation of the Mn^{2+}-containing layers results in low-dimensional magnetic behavior. $Cs_2Mn_3U_6O_{22}$ contains diamagnetic U^{6+} ions as well as high-spin Mn^{2+} (d^5, S = 5/2) ions (see below). The temperature-dependent magnetic susceptibility $\chi(T)$ of $Cs_2Mn_3U_6O_{22}$ was measured under an applied field of 1000 Oe on a sample consisting of ground crystals (Figure 6a). The

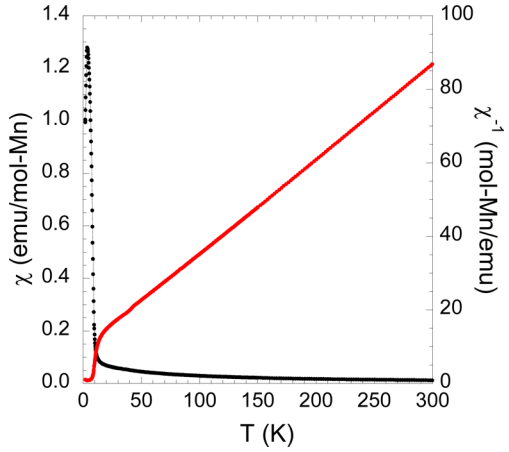

Figure 6. Magnetic susceptibility and inverse susceptibility of $Cs_2Mn_3U_6O_{30}$ measured as a function of temperature on a polycrystalline sample in an applied field of 1000 Oe.

inverse susceptibility versus temperature data from 50−300 K were fitted to a modified Curie−Weiss law

$$\chi(T) = \frac{C}{T - \theta} + \chi_0 \quad (2)$$

where χ_0 is the temperature-independent contribution term, θ is the Weiss temperature, and C is the Curie constant. Our analysis yields a χ_0 of −0.000 45 emu/mol Mn and an effective magnetic moment of $Cs_2Mn_3U_6O_{22}$, μ_{eff} = 5.71 μ_B, which compares well with the calculated moment for high-spin Mn^{2+} (S = 5/2) of 5.91 μ_B. The Curie−Weiss temperature θ = −41 K suggests the presence of predominant antiferromagnetic interactions; however, a ferromagnetic-like magnetic transition is observed at ∼12 K, followed by a downturn at ∼5 K. Repeating the measurement in different applied fields (Figure 7), we observe that the first transition shifts toward higher

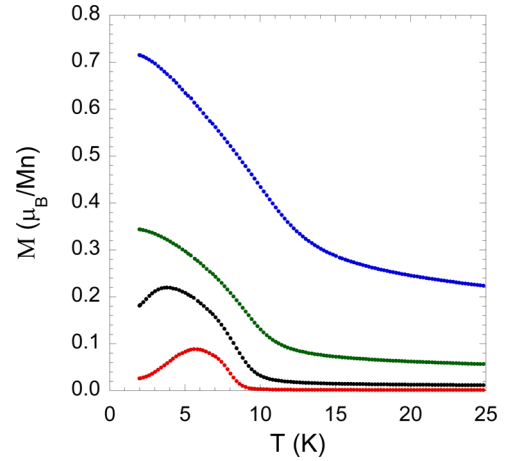

Figure 7. Magnetic susceptibility of $Cs_2Mn_3U_6O_{30}$ measured as a function of temperature in applied fields of 100 (red), 1000 (black), 5000 (green) and 20 000 (blue) Oe.

temperatures, from 9 K at 100 Oe to 14 K at 20 000 Oe, while at the same time the second transition is suppressed. While a distinct downturn at 5 K is observed for the 100 Oe data, no downturn is observed in the 20 000 Oe data down to 2 K.

Because of the plate-shaped morphology of the crystals and the highly anisotropic crystal structure, it was of interest to

DOI: 10.1021/acs.inorgchem.5b00552
Inorg. Chem. 2015, 54, 5495−5503

measure the magnetic susceptibility as a function of sample orientation. Several plate-shaped crystals weighing ~0.4 mg were stacked onto a strip of Kapton tape using GE 7031 Varnish and oriented either parallel or perpendicular to the applied field of 1000 Oe. To compare the oriented single-crystal data with measurements made on polycrystalline powders, the data at 300 K were set to the polycrystalline sample value, and the remainder were normalized accordingly. When the crystals are oriented so that their crystallographic *c*-axis is parallel to the applied field, the susceptibility below 12 K exhibits the same strong ferromagnetic-like transition that is observed for the polycrystalline sample, however, with a maximum susceptibility almost three times larger (Figure 8).

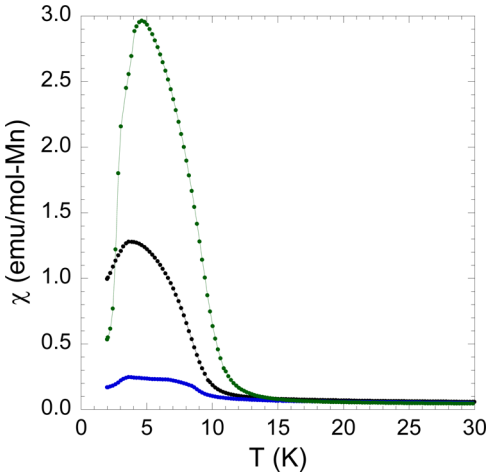

Figure 8. Magnetic susceptibility of a single plate crystal of $Cs_2Mn_3U_6O_{30}$ measured with the crystallographic *c*-axis parallel to the applied field (green) and with the crystallographic *c*-axis perpendicular to the applied field (blue). For comparison, the data for the polycrystalline sample is shown (black).

Below 5 K, an antiferromagnetic downturn is observed, and the susceptibility decreases almost to zero. By contrast, when the plate crystals are oriented parallel, so that their crystallographic *c*-axis is perpendicular to the applied field, only a very weak increase at 12 K and subsequent decrease at 5 K in the susceptibility is observed. Because of the difficulty in positioning the crystal exactly parallel to the applied field, it is likely that magnetic susceptibility for the crystal in this orientation is virtually unchanged with temperature and that the observed signal is due to a slight orientation misalignment.

The magnetic susceptibility data collected under both FC and ZFC conditions are presented in Figure 9. The FC and ZFC data of the polycrystalline sample overlay almost perfectly. The ZFC and FC data for the oriented single crystals show a small deviation between the two measurements at temperatures below 10 K, indicating the existence of a slight amount of field dependence in the low-temperature regime.

C. Spin Exchange Interactions and Magnetic Structure. To account for the observed magnetic properties of $Cs_2Mn_3U_6O_{22}$, we examine its spin exchange interactions by using its crystal structure optimized by DFT+U calculations. As shown in Figures 10a and 10b we consider nine spin exchange

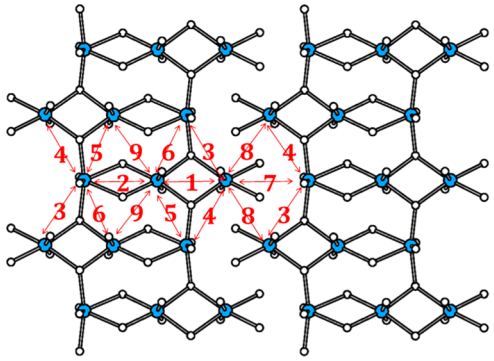

Figure 10a. Illustration of nine spin exchange paths $J_1 - J_9$ used to calculate the spin exchange interactions using its crystal structure optimized by DFT+U calculations.

paths $J_1 - J_9$, whose geometrical parameters are listed in Table 4. To extract the values of $J_1 - J_9$, we examine the relative energies of the 10 ordered spin arrangements defined using a (2*a*, *b*, *c*) supercell (Supporting Information, Figure S4) on the basis of the DFT+U calculations with U^{eff} = 4, 5, and 6 eV and with 2 × 2 × 2 k-points. In terms of $J_1 - J_9$, the total spin exchange energies per (2*a*, *b*, *c*) supercell of the 10 states are expressed as

$$(n_1J_1 + n_2J_2 + n_3J_3 + n_4J_4 + n_5J_5 + n_6J_6 + n_7J_7 + n_8J_8 + n_9J_9)(N^2/4) \quad (3)$$

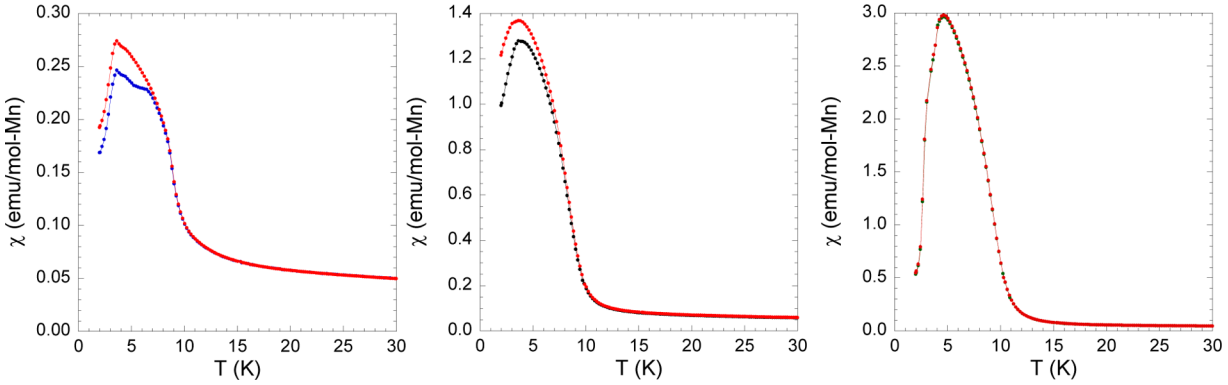

Figure 9. FC and ZFC magnetic susceptibility of a single plate crystal of $Cs_2Mn_3U_6O_{30}$ measured with the crystallographic *c*-axis perpendicular to the applied field (left) and with the crystallographic *c*-axis parallel to the applied field (middle). For comparison, the data for the polycrystalline sample is shown (right).

DOI: 10.1021/acs.inorgchem.5b00552
Inorg. Chem. 2015, 54, 5495−5503

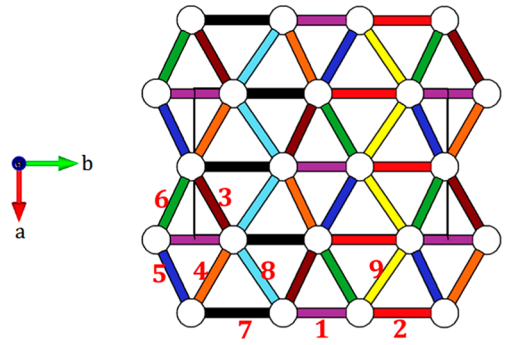

Figure 10b. Illustration of relative energies of the 10 ordered spin arrangements defined using a (2*a*, *b*, *c*) supercell.

Table 4. Geometrical Parameters of the Nine Spin Exchange Paths Defined in Figure 10b

exchange path	Mn···Mn (Å)	Mn−O (Å)	∠Mn−O−Mn (deg)
J_1	3.585	2.370, 2.329	99.44
		2.378, 2.325	99.34
J_2	3.835	2.232, 2.404	111.59
		2.230, 2.395	111.96
J_3	3.993	2.370, 2.188	122.32
J_4	4.015	2.378, 2.189	123.00
J_5	3.754	2.325, 2.189	112.52
		2.676, 2.395	95.35
J_6	3.769	2.329, 2.188	113.08
		2.682, 2.404	95.48
J_7	4.352	2.211, 2.902	116.00
		2.211, 2.888	116.57
J_8	4.133	2.678, 2.211	115.12
		2.211, 2.670	115.45
J_9	4.138	2.682, 2.232	114.40
		2.230, 2.676	114.70

where N refers to the number of unpaired spins on Mn^{2+} (N = 5 in the present case). The values of $n_1 - n_9$ for the 10 ordered spin states are summarized in Supporting Information, Table S3. The relative energies per (2*a*, *b*, *c*) supercell of the 10 ordered spin states determined by DFT+U calculations with U^{eff} = 4, 5, and 6 eV are summarized in Supporting Information, Table S4. Then, by mapping the relative energies of the DFT+U calculations onto those of the above spin exchange energies,[45−48] we obtain the values of $J_1 - J_9$ summarized in Table 5. In the mean-field theory,[49] the Curie−Weiss temperature θ is related to the spin exchange parameters as follows:

Table 5. Values (in meV) of the spin exchanges $J_1 - J_9$ determined from DFT+U Calculations

	U_{eff} = 4 eV	U_{eff} = 5 eV	U_{eff} = 6 eV
J_1	−0.018	0.006	0.022
J_2	−0.210	−0.156	−0.114
J_3	−0.207	−0.150	−0.106
J_4	−0.203	−0.147	−0.103
J_5	−0.104	−0.063	−0.032
J_6	−0.104	−0.063	−0.032
J_7	−0.213	−0.170	−0.136
J_8	−0.141	−0.114	−0.093
J_9	−0.189	−0.151	−0.120

$$\theta = \frac{S(S+1)}{3k_B} \sum_i z_i J_i \tag{4a}$$

where the summation runs over all nearest neighbors for a given spin site, z_i is the number of nearest neighbors connected by the spin exchange parameter J_i, and S is the spin quantum number of each spin site (i.e., S = 5/2 for high-spin Mn^{2+}). As can be seen from Figure 10, the summation for $Cs_2Mn_3U_6O_{22}$ can be calculated at three different sites leading to different results. Thus, by averaging these three contributions, we obtain

$$\theta \approx 5(J_1 + J_2 + J_3 + J_4 + J_5 + J_6 + J_7 + J_8 + J_9)/k_B \tag{4b}$$

Then, the θ values are estimated to be −31, −23, and −16 K from the spin exchanges obtained from the DFT+U calculations with U^{eff} = 4, 5, and 6 eV, respectively. Thus, the spin exchanges obtained for DFT+U calculations with U^{eff} = 4 eV are most appropriate for $Cs_2Mn_3U_6O_{22}$.

We now consider a probable cause for the sharp susceptibility peak around 15 K (Figure 6). Our calculations show that, of the nine spin exchanges, only three (namely, J_1, J_5, and J_6) are weak compared with the remainder. Thus, if we neglect these three weak interactions, we obtain the spin−lattice presented in Figure 11, which has two-leg spin ladders

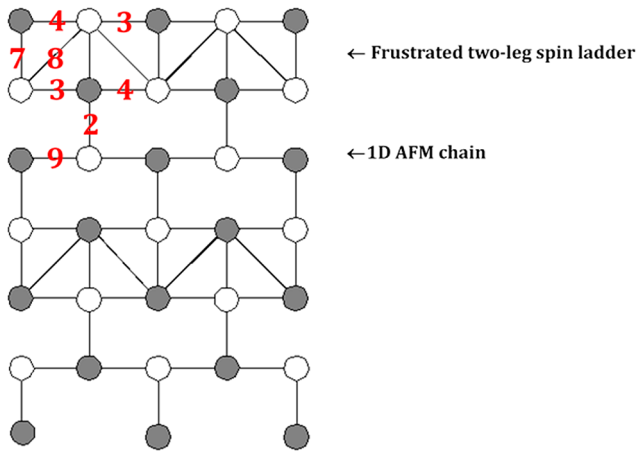

Figure 11. Illustration of the spin−lattice consisting of two-leg spin ladders made up of J_3, J_4, and J_7 as well as chains made up of J_9.

made up of J_3, J_4, and J_7 as well as chains made up of J_9. These ladders and chains are interconnected by J_2. All these five spin exchanges can be antiferromagnetically coupled. Then the spin ladders have spin frustration arising from J_8. This spin frustration can give rise to a weak spin canting in the two-leg spin ladders, which would lead to a nonzero moment and hence to a sharp increase in the magnetic susceptibility. Then, the difference between the FC and ZFC magnetic susceptibilities below 15 K would be a consequence of forming weakly ferromagnetic domains.

4. CONCLUDING REMARKS

The quaternary uranium-containing oxide $Cs_2Mn_3U_6O_{22}$ was crystallized out of a reactive cesium chloride flux, where crystal growth was enhanced via the evaporation of the flux at high temperature. $Cs_2Mn_3U_6O_{22}$ forms in a novel layered structure type consisting of $Mn_3U_6O_{22}^{2-}$ slabs separated by layers of cesium atoms. This ordered arrangement creates a separation between manganese layers of 13 Å, leading to two-dimensional

DOI: 10.1021/acs.inorgchem.5b00552
Inorg. Chem. 2015, 54, 5495−5503

magnetic properties. $Cs_2Mn_3U_6O_{22}$ exhibits low-dimensional magnetic interactions that are best described as a spin−lattice consisting of frustrated two-leg spin ladders combined with one-dimensional AFM chains. The observed sharp increase in the magnetic susceptibility should be considered as arising from spin canting.

■ ASSOCIATED CONTENT

Supporting Information

X-ray data in CIF format, powder XRD patterns, and electron difference data. Additional structure images and images of the ordered spin states. Tabulated anisotropic displacement parameters and optimized atomic positions. These materials are free of charge via the Internet at The Supporting Information is available free of charge on the ACS Publications website at DOI: 10.1021/acs.inorgchem.5b00552.

■ AUTHOR INFORMATION

Corresponding Author

*E-mail: zurloye@mailbox.sc.edu.

Notes

The authors declare no competing financial interest.

■ ACKNOWLEDGMENTS

Research supported by the U.S. Department of Energy, Office of Basic Energy Sciences, Division of Materials Sciences and Engineering under Award No. DE-SC0008664. The investigation of the electronic and magnetic structures by first-principles DFT calculations performed at NCSU were supported by the computing resources of the NERSC Center and the HPC Center of NCSU.

■ REFERENCES

(1) Aruta, C.; Licci, F.; Zappettini, A.; Bolzoni, F.; Rastelli, F.; Ferro, P.; Besagni, T. *Appl. Phys. A: Mater. Sci. Process.* **2005**, *81*, 963−968.
(2) Chi, L.; Britten, J. F.; Greedan, J. E. *J. Solid State Chem.* **2003**, *172*, 451−457.
(3) Cuthbert, H. L.; Greedan, J. E.; Vargas-Baca, I.; Derakhshan, S.; Swainson, I. P. *Inorg. Chem.* **2007**, *46*, 8739−8745.
(4) Greenblatt, M. *Chem. Rev.* **1988**, *88*, 31−53.
(5) Hu, S.; Johnsson, M.; Law, J. M.; Bettis, J. L. J.; Whangbo, M.-H.; Kremer, R. K. *Inorg. Chem.* **2014**, *53*, 4250−4256.
(6) Kim, K.-H.; Kim, H.-J.; Lee, S.-I.; Iyo, A.; Tanaka, Y.; Tokiwa, K.; Watanabe, T. *Phys. Rev. B* **2004**, *70*, 092501.
(7) Nénert, G.; Isobe, M.; Kim, I.; Ritter, C.; Colin, C. V.; Vasiliev, A. N.; Kim, K. H.; Ueda, Y. *Phys. Rev. B* **2010**, *82*, 024429.
(8) Wang, Z.; Jain, P.; Choi, K.-Y.; van, T.; Johan; Cheetham, A. K.; Kroto, H. W.; Koo, H.-J.; Zhou, H.; Hwang, J.; Choi, E. S.; Whangbo, M.-H.; Dalal, N. S. *Phys. Rev. B* **2013**, *87*, 224406.
(9) Bouloux, J.-C.; Soubeyroux, J.-L.; Le Flem, G.; Hagenguller, P. *J. Solid State Chem.* **1981**, *38*, 34−39.
(10) Castillo-Martínez, E.; Alario-Franco, M.Á. *Solid State Sci.* **2007**, *9*, 564−573.
(11) David, R.; Pautrat, A.; Filimonov, D.; Kabbour, H.; Vezin, H.; Whangbo, M.-H.; Mentre, O. *J. Am. Chem. Soc.* **2013**, *135*, 13023−13029.
(12) Liu, G.; Greedan, J. E. *J. Solid State Chem.* **1995**, *114*, 499−505.
(13) Paul, S.; Ghosh, A.; Sato, T.; Sarma, D. D.; Takahashi, T.; Wang, E.; Greenblatt, M.; Raj, S. *Europhys. Lett.* **2014**, *105*, 47003.
(14) Poltavets, V. V.; Lokshin, K. A.; Nevidomskyy, A. H.; Croft, M.; Tyson, T. A.; Hadermann, J.; Van Tendeloo, G.; Egami, T.; Kotliar, G.; ApRoberts-Warren, N.; Dioguardi, A. P.; Curro, N. J.; Greenblatt, M. *Phys. Rev. Lett.* **2010**, *104*, 206403.
(15) Wiebe, C. R.; Russo, P. L.; Savici, A. T.; Uemura, Y. J.; MacDougall, G. J.; Luke, G. M.; Kuchta, S.; Greedan, J. E. *J. Phys.: Condens. Matter* **2005**, *17*, 6469−6482.
(16) Yeon, J.; Sefat, A. S.; Tran, T. T.; Halasyamani, P. S.; zur Loye, H.-C. *Inorg. Chem.* **2013**, *52*, 6179−6186.
(17) Onsager, L. *Phys. Rev.* **1944**, *65*, 117−149.
(18) Burns, P. C. *Can. Mineral.* **2005**, *43*, 1839−1984.
(19) Read, C. M. Discovery of Novel Uranium-Containing Oxides and Related Materials by Flux Crystal Growth. Ph.D. Thesis, The University of South Carolina, May 2015.
(20) Read, C. M.; Yeon, J.; Smith, M. D.; zur Loye, H.-C. *CrystEngComm* **2014**, *16*, 7259−7267.
(21) Bugaris, D. E.; zur Loye, H.-C. *Angew. Chem., Int. Ed. Engl.* **2012**, *51*, 3780−3811.
(22) Obbade, S.; Dion, C.; Bekaert, E.; Yagoubi, S.; Saadi, M.; Abraham, F. *J. Solid State Chem.* **2003**, *172*, 305−318.
(23) Obbade, S.; Yagoubi, S.; Dion, C.; Saadi, M.; Abraham, F. *J. Solid State Chem.* **2003**, *174*, 19−31.
(24) Read, C. M.; Bugaris, D. E.; zur Loye, H.-C. *Solid State Sci.* **2013**, *17*, 40−45.
(25) Read, C. M.; Smith, M. D.; zur Loye, H.-C. *J. Chem. Crystallogr.* **2013**, *43*, 484−487.
(26) Roof, I. P.; Smith, M. D.; zur Loye, H.-C. *J. Cryst. Growth* **2010**, *312*, 1240−1243.
(27) Roof, I. P.; Smith, M. D.; zur Loye, H.-C. *Solid State Sci.* **2010**, *12*, 1941−1947.
(28) Roof, I. P.; Smith, M. D.; zur Loye, H.-C. *J. Chem. Crystallogr.* **2010**, *40*, 491−495.
(29) Read, C. M.; Smith, M. D.; zur Loye, H.-C. *Solid State Sci.* **2014**, *37*, 136−143.
(30) Babo, J.-M.; Albrecht-Schmitt, T. E. *J. Solid State Chem.* **2013**, *197*, 186−190.
(31) Dion, C.; Obbade, S.; Raekelboom, E.; Abraham, F.; Saadi, M. *J. Solid State Chem.* **2000**, *155*, 342−353.
(32) Obbade, S.; Dion, C.; Duvieubourg, L.; Saadi, M.; Abraham, F. *J. Solid State Chem.* **2003**, *173*, 1−12.
(33) Read, C. M.; Smith, M. D.; zur Loye, H.-C. *J. Chem. Crystallogr.* **2014**, *44*, 604−608.
(34) *SMART Version 5.630, SAINT+ Version 6.45, SADABS Version 2.10;* Bruker Analytical X-ray Systems, Inc.: Madison, WI, 2003.
(35) Sheldrick, G. M. *Acta Crystallogr., Sect. A* **2008**, *64*, 112−122.
(36) Dolomanov, O. V.; Bourhis, L. J.; Gildea, R. J.; Howard, J. A. K.; Puschmann, H. *J. Appl. Crystallogr.* **2009**, *42*, 339−341.
(37) Morrison, G.; zur Loye, H.-C. *J. Solid State Chem.* **2015**, *221*, 334−337.
(38) Kresse, G.; Furthmüller, J. *Phys. Rev. B* **1996**, *54*, 11169.
(39) Kresse, G.; Hafner, J. *Phys. Rev. B* **1993**, *47*, 558.
(40) Kresse, G.; Furthmüller, J. *Comput. Mater. Sci.* **1996**, *6*, 15−50.
(41) Perdew, J. P.; Burke, K.; Ernzerhof, M. *Phys. Rev. Lett.* **1996**, *77*, 3865.
(42) Dudarev, S. L.; Botton, G. A.; Savrasov, S. Y.; Hurmphreys, C. J.; Sutton, A. P. *Phys. Rev. B* **1998**, *57*, 1505.
(43) Hannerz, H.; Svensson, G.; Esmaeilzadeh, S.; Grins, J. *Solid State Sci.* **1999**, *1*, 567−575.
(44) Brown, I. D.; Altermatt, D. *Acta Crystallogr., Sect. B* **1985**, *41*, 244−247.
(45) Whangbo, M.-H.; Koo, H.-J.; Dai, D. *J. Solid State Chem.* **2003**, *176*, 417−481.
(46) Dai, D.; Whangbo, M.-H. *J. Chem. Phys.* **2001**, *114*, 2887−2893.
(47) Dai, D.; Whangbo, M.-H. *J. Chem. Phys.* **2003**, *118*, 29−39.
(48) Xiang, H. J.; Lee, C.; Koo, H.-J.; Whangbo, M.-H. *Dalton Trans.* **2013**, *42*, 823−853.
(49) Smart, S. J. *Effective Field Theory of Magnetism;* Saunders: Philadelphia, PA, 1966.

DOI: 10.1021/acs.inorgchem.5b00552
Inorg. Chem. 2015, 54, 5495−5503